Check for updates

Simulations of structure formation by confined dipolar active particles

Vitali Telezki [iD] * and Stefan Klumpp [iD]

Dipolar active particles describe a class of self-propelled, biological or artificial particles equipped with an internal (typically magnetic) dipole moment. Because of the interplay between self-propulsion and dipole−dipole interactions, complex collective behavior is expected to emerge in systems of such particles. Here, we use Brownian dynamics simulations to explore this collective behavior. We focus on the structures that form in small systems in spatial confinement. We quantify the type of structures that emerge and how they depend on the self-propulsion speed and the dipolar (magnetic) strength of the particles. We observe that the dipolar active particles self-assemble into chains and rings. The dominant configuration is quantified with an order parameter for chain and ring formation and shown to depend on the self-propulsion speed and the dipolar magnetic strength of the particles. In addition, we show that the structural configurations are also affected by the confining walls. To that end, we compare different confining geometries and study the impact of a reorienting 'wall torque' upon collisions of a particle with a wall. Our results indicate that dipolar interactions can further enhance the already rich variety of collective behaviors of active particles.

1 Introduction

Self-propelled active particles that convert energy from their environment into directed motion are known to exhibit rich collective behavior such as self-organized pattern formation or swarming due to an interplay between various interaction forces.[1–3] Microscopic active particles in fluids, so-called microswimmers, have been a particular focus of research both because of their rich dynamics[4] and because of their potential in biomedical applications.[5,6]

From an application point of view, an important feature of active particles is their accessibility to remote control. In that respect, magnetic active particles, which possess a magnetic dipole moment, specifically magnetic microswimmers, are of interest as they can be controlled by external magnetic fields. A biological example of a dipolar microswimmer is given by magnetotactic bacteria.[7–11] These bacteria orient in external magnetic fields[12] with the help of the magnetosome chain, a chain of iron-oxide nanocrystals inside their cell body.[13] Proof-of-principle applications have demonstrated that magnetotactic bacteria can be utilized in drug delivery applications and cancer treatment.[14–16] Examples for artificial dipolar microswimmers are magnetic Janus particles that can self-assemble into various structures that are controllable with

external magnetic fields[17,18] and various types of magnetic microrobots.[19,20] While the dipole moment of these active particles provides a way to address them externally for steering, it generally also introduces dipole–dipole interactions between the active particles and can thus give rise to new forms of collective behavior, including spatial patterns.

Self-assembly of dipolar passive particles in small systems[21] and in large systems has been studied theoretically,[22–24] partly motivated by observations in ferrofluids.[25–27] Small passive systems are known to form chains ($N \leq 3$), rings ($3 < N \leq 17$) or more complex, concentric multi-shell hexagonal patterns ($N \geq 18$) as energetically favorable configurations in two dimensions.[28–32]

Dipolar coupling between active dipolar particles has recently been studied by several groups. Guzmán-Lastra *et al.* have investigated the hydrodynamic flow fields of self-assembled microswimmers. In particular, they studied how hydrodynamic and magnetic interactions affect cluster formation.[33] In another study by Liao *et al.* the effect of motility and dipolar interactions on cluster formation has been investigated. In their Brownian dynamics simulations, they observed formation of chain-like structures and that motility-induced phase separation (MIPS) is generally suppressed by dipolar interactions.[24]

Most of these studies have focused on the collective behavior in spatially homogeneous environments. However, the motion of active microswimmers is often confined either by their natural environment like interfacial barriers or by complex

Institute for the Dynamics of Complex Systems, Georg August University Göttingen, Friedrich-Hund-Platz 1, 37077 Göttingen, Germany.
E-mail: vitali.telezki@theorie.physik.uni-goettingen.de; Tel: +49551 3926946

experimental setups like microfluidic devices. Such confinement has been shown to affect the motion of active particles *via* steric and/or hydrodynamic interactions[34–39] and to result in novel patterns of motion.[40–42] Moreover, in many scenarios for applications, the number of active particles is typically rather small.

Therefore, here we study structure formation of dipolar active particles in small systems that are spatially confined. To that end, we use an active Brownian particle model and equip the particles with a dipole moment and dipole–dipole interactions. The corresponding Langevin equations for the position and orientation of the active particles are solved numerically in two dimensions. We do not consider hydrodynamic interactions between the particles, but hydrodynamic interactions with the confining walls may be included *via* a phenomenological wall torque. Using this model, we ask what structures (such as chains and rings) emerge and how these structures are affected by motility and magnetic interactions as well as by the geometry of the confining chamber and by the interactions of the swimmer with the confining walls.

2 Model

2.1 Equations of motion

In our model, we consider active Brownian spheres in two dimensions that have a permanent dipole moment $\boldsymbol{\mu}_i = \mu \hat{\boldsymbol{e}}_i$ with the magnetic strength μ at the particle center. Here and in the following, the superscript 'hat' denotes a unit vector. The magnetic moment is aligned with the orientation of the particle $\hat{\boldsymbol{e}}_i$, which defines the direction of self-propulsion with speed v_0. The equations of motion for a particle i with position $\boldsymbol{r}_i$ and orientation $\hat{\boldsymbol{e}}_i$ are given by

$$\dot{\boldsymbol{r}}_i = v_0\hat{\boldsymbol{e}}_i + \frac{1}{\gamma_{\mathrm{T}}}\boldsymbol{F}_i + \sqrt{2D_{\mathrm{T}}}\,\xi_i^{\mathrm{T}} \tag{1}$$

$$\dot{\hat{\boldsymbol{e}}}_i = \frac{1}{\gamma_{\mathrm{R}}}\boldsymbol{\tau}_i \times \hat{\boldsymbol{e}}_i + \sqrt{2D_{\mathrm{R}}}\,\xi_i^{\mathrm{R}} \times \hat{\boldsymbol{e}}_i, \tag{2}$$

where γ_{T} and γ_{R} are the translational and rotational drag coefficients, ξ_i^{T} is the translational stochastic force, and ξ_i^{R} is the rotational stochastic torque. Both are described by Gaussian white noise with zero mean

$$\langle \boldsymbol{\xi}^{\mathrm{T,R}} \rangle = 0$$

$$\langle \boldsymbol{\xi}^{\mathrm{T,R}}(t) \cdot \boldsymbol{\xi}^{\mathrm{T,R}}(t') \rangle = \mathbf{1}\delta(t - t').$$

D_{T} and D_{R} are the corresponding diffusion coefficients. $\boldsymbol{F}_i$ and $\boldsymbol{\tau}_i$ describe forces and torques acting on particle i. The forces $\boldsymbol{F}_i$ acting on particle i are given by the sum of the particle–particle interactions and the interactions with the confining walls of the system,

$$\boldsymbol{F}_i = \sum_{i \neq j}\left(\boldsymbol{F}_{ij}^{\mathrm{dd}} + \boldsymbol{F}_{ij}^{\mathrm{WCA}}\right) + \boldsymbol{F}_i^{\mathrm{wall}}.$$

The pairwise forces between two particles i, j separated by the distance $r_{ij} = |\boldsymbol{r}_{ij}| = |\boldsymbol{r}_i - \boldsymbol{r}_j|$ consist of dipolar forces

and excluded volume interactions. The dipolar forces are given by[43]

$$\boldsymbol{F}_{ij}^{\mathrm{dd}} = \frac{3\mu_0\mu^2}{4\pi r_{ij}^4}\big[\hat{\boldsymbol{r}}_{ij}(\hat{\boldsymbol{e}}_i \cdot \hat{\boldsymbol{e}}_j) + \hat{\boldsymbol{e}}_i(\hat{\boldsymbol{r}}_{ij} \cdot \hat{\boldsymbol{e}}_j) + \hat{\boldsymbol{e}}_j(\hat{\boldsymbol{r}}_{ij} \cdot \hat{\boldsymbol{e}}_i)$$
$$-5\hat{\boldsymbol{r}}_{ij}(\hat{\boldsymbol{r}}_{ij} \cdot \hat{\boldsymbol{e}}_i)(\hat{\boldsymbol{r}}_{ij} \cdot \hat{\boldsymbol{e}}_j)\big].$$

The excluded volume interactions are modeled by the Weeks–Chandler–Anderson (WCA)[44] pair potential with the interaction energy ε and the particle diameter σ

$$\boldsymbol{F}_{ij}^{\mathrm{WCA}} = \begin{cases} 48\varepsilon\dfrac{r_{ij}}{r_{ij}^2}\left[\left(\dfrac{\sigma}{r_{ij}}\right)^{12} - \dfrac{1}{2}\left(\dfrac{\sigma}{r_{ij}}\right)^6\right] & \text{if } r_{ij} < 2^{1/6}\sigma \\ 0 & \text{if } r_{ij} \geq 2^{1/6}\sigma. \end{cases}$$

Forces resulting from interactions with the confinement $\boldsymbol{F}_i^{\mathrm{wall}}$ are described by the same WCA potential by calculating the shortest distance to the wall and applying the repulsive force for a virtual wall particle with its surface at the point of shortest distance (*i.e.* outside the wall at a distance $\frac{\sigma}{2}$). The torques $\boldsymbol{\tau}_i$ acting on the particle i result from the pairwise dipolar interactions and the interactions with the confining walls of the system

$$\boldsymbol{\tau}_i = \boldsymbol{\tau}_i^{\mathrm{wall}} + \sum_{i \neq j}\boldsymbol{\tau}_{ij}^{\mathrm{dd}}.$$

The torques resulting from pairwise dipolar interactions are given by[45]

$$\boldsymbol{\tau}_{ij}^{\mathrm{dd}} = \frac{\mu_0\mu^2}{4\pi r_{ij}^3}\big[3(\hat{\boldsymbol{e}}_i \cdot \hat{\boldsymbol{r}}_{ij})(\hat{\boldsymbol{e}}_j \times \hat{\boldsymbol{r}}_{ij}) + (\hat{\boldsymbol{e}}_i \times \hat{\boldsymbol{e}}_j)\big]$$

with the vacuum permeability μ_0.

Active particles may behave differently when approaching a solid boundary. A combination of hydrodynamic effects, steric interactions between the wall and the swimmers' body or, possibly, their flagella can lead to a reorientation of the swimmer at the wall.[3,41,46,47] To model the reorientation of the swimmers near a wall, we introduce a wall torque $\boldsymbol{\tau}_i^{\mathrm{wall}}$ that can be modified with the tuning parameter α

$$\boldsymbol{\tau}_i^{\mathrm{wall}} = \alpha\hat{\boldsymbol{e}}_i \times \boldsymbol{F}_i^{\mathrm{wall}}. \tag{3}$$

A value of $\alpha = 0$ results in a purely repulsive wall with no reorienting torque.

2.2 Simulation method

We solve the equations of motion in two dimensions by using overdamped Brownian dynamics (BD) simulations. In two dimensions, we can simplify eqn (2) by describing the orientation of the particle with an angle φ in the 2d plane. This leads to

$$\dot{\varphi}_i = \frac{1}{\gamma_{\mathrm{R}}}\tau_i + \sqrt{2D_{\mathrm{R}}}\,\xi_i^{\mathrm{R}}. \tag{4}$$

Thus instead of eqn (1) and (2), we effectively integrate eqn (1) and (4). We note that by this simplification the multiplicative

noise in eqn (2) simplifies to additive noise in eqn (4). The following reduced units were used: time $t^* = tD_0^T/\sigma^2$, where $D_0^T = k_BT/3\pi\eta\sigma$ is the translational diffusion constant; position $r^* = r/\sigma$; temperature $T^* = k_BT/\varepsilon$; field strength $B^* = B/B_0$, where $B_0 = 1 \times 10^{-5}$ T is the order of magnitude of the magnetic field strength of the earth; dipole strength $\mu^* = \mu B_0/\varepsilon$. The dimensionless equations of motion were integrated for $N_{steps} = 5 \times 10^6$ time steps using a 2nd order stochastic Runge–Kutta scheme[48,49] with a time step $\Delta t^* = 2 \times 10^{-5}$. We note that, with this choice of dimensionless units, the self-propulsion velocity $v_0^* = v_0\sigma/D_0^T$ is identical to the Peclét number. For the sake of readability, we will omit the asterisk for dimensionless quantities from now on.

Throughout all simulations the temperature of the system was set to $T = 1$, while varying the self-propulsion speed v_0 and the magnetic strength μ of the swimmers. To investigate the effect of the geometry of the confinement, the simulations were run both in squared confinement with a side length $L = 50$ and circular confinement with a radius $R = L/\sqrt{\pi}$ to match the area of the squared confinement. The simulations were performed for $N = 36$ (filling fraction $\Phi = 0.01$) and $N = 81$ particles ($\Phi = 0.03$) respectively, while varying the geometry of the confinement and the wall torque parameter α. To investigate the effect of density, the side length of the quadratic confinement with $\alpha = 0$ was reduced to $L = 33.3$ ($\Phi = 0.03$, matching the density of $N = 81$ particles) and $L = 16.8$ ($\Phi = 0.1$). The particles were initially placed on a regular quadratic grid. For statistical analysis the first 1×10^6 time steps of the trajectories were omitted. The trajectories were analyzed every 6000 time steps.

3 Results

3.1 Assembly of chain and ring structures

We first investigated the dynamics of dipolar swimmers in a squared confinement (i.e., with repulsive walls) without wall-induced torques ($\alpha = 0$) for a small number of swimmers ($N = 36$). A cut-out of a typical snapshot of the simulation is shown in Fig. 1. In the simulations we observed that for certain parameters dipolar swimmers self-assemble into polymers. These polymers can mainly adopt two structural formations: chains (Fig. 1a and c) and rings (Fig. 1b). We observed that individual dipolar swimmers usually first self-assemble into a chain which then eventually catches its own tail and forms a ring. These structures are dynamic; rings and chains can disassemble again into chains, smaller chains or individual monomers. The number of dipolar swimmers in one structure varies. Generally, we observed that the structure depends on the magnetic strength μ, the self-propulsion speed v_0 and the boundary conditions.

To quantify the formation of these structures, we asked what the probability of structure formation p_s is and how it depends on the magnetic strength μ and the self-propulsion speed v_0. To answer that question, we identified particle clusters using a density based cluster algorithm (DBSCAN[50]), where the closest neighbor distance was set to $\varepsilon = 1.21\sigma$ and the minimal number
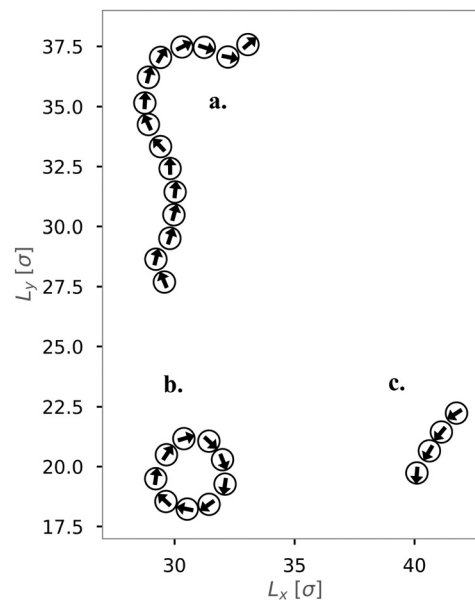

Fig. 1 Detail of a snapshot at time $t = 21.92$ for a simulation with $v_0 = 5$, $\mu = 1.2$ in a squared simulation box with $L = 50$ and $\alpha = 0$. The magnetic moment of the dipolar swimmer is represented as a black arrow. Different structures are visible: a long chain (a), a ring (b) and a short chain (c).

of particles in a neighborhood to form a cluster was set to $N = 3$ which is similar to other studies.[24,51] The value of ε was determined by analysing the nearest neighbor distance $g_1(r)$, for $\mu = 1$ (see Fig. 2). This choice of the magnetic strength $\mu = 1$ corresponds to a dipolar coupling strength of $\lambda = \mu^2/T = 1$ where the pair-wise dipole interactions start becoming relevant. The histograms indicate that the closest neighbor distance weakly depends on the self-propulsion speed v_0. Here, $\varepsilon = 1.21\sigma$ is highlighted by the dotted line. This value of ε was chosen as more than 85% of the particles lay in this region for all three choices of the self-propulsion velocity.

The probability of structure formation is then defined as the number of particles associated with a cluster divided by the total number of particles in the simulation per snapshot, averaged over 10 realizations. This parameter is also known as the degree of polymerization.[51–53] The result is shown in Fig. 3 for different self-propulsion speeds v_0. Here, we observe a
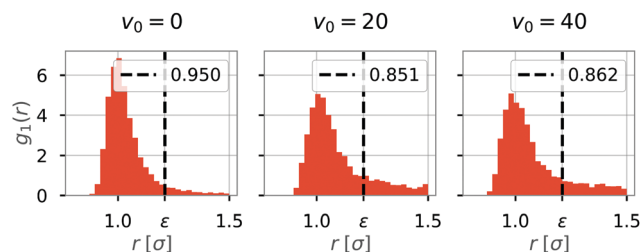

Fig. 2 Normalized histograms of the nearest neighbor distance $g_1(r)$ for dipolar swimmers with $\mu = 1$ and different self-propulsion speeds v_0. The dotted line is drawn at $\varepsilon = 1.21\sigma$. The number in the top right shows the fraction of accumulated counts up to the dotted line. Data taken from 10 simulation runs in quadratic confinement with $L = 50$ and $\alpha = 0$.
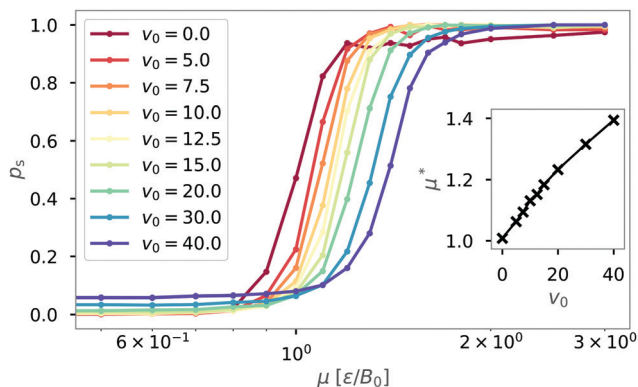
Fig. 3 Semi-logarithmic curves of the probability of structure formation p_s as a function of the magnetic strength μ for N = 36 particles. The different curves correspond to different self-propulsion speeds v_0. The inset shows the dependence of the critical magnetic strength $\mu^\star$ on the self-propulsion speed. Data taken from 10 simulation runs in quadratic confinement with L = 50 and α = 0.

steep increase of the probability of structure formation p_s with increasing magnetic strength μ. This steep increase suggests that a critical value $\mu^\star$ for the magnetic strength can be defined. We estimate such critical value by calculating $p_s(\mu^\star)$ = 0.5 *via* linear interpolation between the two data points closest to p_s = 0.5. The inset shows that the critical magnetic strength $\mu^\star$ increases approximately linearly with the self-propulsion speed v_0. We note that the critical value of $\mu^\star \approx 1.0$ for passive particles (v_0 = 0) corresponds to a dipolar coupling strength of $\lambda = \mu^{\star 2}/T = 1$. For passive particles, the ratio between pairwise dipolar coupling energy and thermal energy is the only relevant parameter for structure formation. Structures begin to dominate ($p_s > 0.5$) exactly when dipolar coupling energy between two particles matches the thermal energy of the system ($\mu^{\star 2} = T$). Adding activity to the system increases the drive towards disorder and thus requires stronger dipolar interactions for structures to form. The linear dependence seen in Fig. 3 suggests a correction to the critical magnetic coupling strength which is linear in first order $\mu^\star = \sqrt{T}(1 + \gamma v_0)$ with a constant γ. Such a correction is obtained quite generally if the balance condition $\lambda = 1$ or $\mu^{\star 2} = T$ is modified to $\mu^{\star 2} = T + f(v_0)$, where the second term (with $f'(0) = \gamma$) describes the additional 'noise' due to active motion.

3.2 Classification of structures

After determining the probability that a structure assembles, we classified the types of structures (*i.e.* chains and rings) that are observed. To classify the type of structures in a quantitative manner, we introduce the order parameter C. Fig. 4 illustrates how the order parameter C is calculated. After each cluster has been identified (see Fig. 4a shades of blue), a shortest-path algorithm[54] was used to determine the contour length l (red) of the cluster as well as the head–tail distance d of the cluster. The order parameter C describes the distance d between head and tail of the cluster normalized to its contour length l while accounting for excluded volume interactions
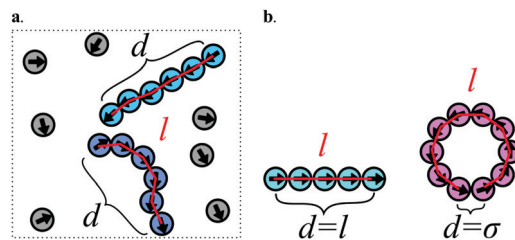

Fig. 4 (a) Illustration showing how the order parameter C is calculated. Particles in different shades of blue belong to different clusters, gray particles are not in a cluster. The red line indicates the contour length l, while d is the head–tail distance. The particle orientation is indicated by arrows. (b) Example of two extreme configurations: a completely straight chain (turquoise), where the head–tail distance d is equal to the contour length l and a perfect ring (pink), where the head–tail distance d is equal to the particle diameter σ.

which lead to a minimal possible distance of σ between two particles:

$$C = 1 - \frac{d - \sigma}{l - \sigma}. \tag{5}$$

Following this definition, a completely straight chain (Fig. 4b turquoise) with minimal neighbor distance σ results in the order parameter C = 0, while a fully closed ring (pink) results in C = 1.

Here, we ask the question what value of the order parameter represents the system the best for given self-propulsion speed and magnetic strength. Do we observe structures and if yes, are they more likely to be chains or rings?

To answer this question, we investigate the distribution of the order parameter C while varying the magnetic strength and the self-propulsion speed of the dipolar swimmer. Fig. 5 shows examples of the cluster size weighted histograms for different
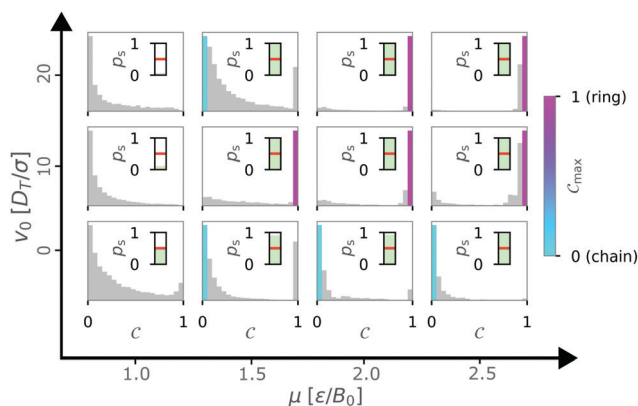

Fig. 5 State weighted histograms for N = 36 particles in a quadratic box with L = 50 and α = 0 show bimodal distributions of the order parameter C for different parameters. The maximum of the histogram is found either at C_{max} = 1 or at C_{max} = 0. These cases correspond to a ring or chain structure and are colored in pink and turquoise, respectively. The inset shows the probability of structure formation, where the red line indicates the value p_s = 0.5. If $p_s < 0.5$, the system is considered as predominantly unstructured and all bars are shown in gray. Data taken from 10 simulation runs.

simulation parameters. Each histogram is based on 10 independent realizations. We observed that the maxima of the distributions are binary, located at either $C = 0$ or $C = 1$ for the case of quadratic confinement with $\alpha = 0$.

To find the most representative state, we first determined whether more states without a structure than with a structure were counted. If we counted more states with a structure ($p_s > 0.5$), we determined which structure occurred most frequently by calculating the maximum C_{max} (*e.g.* colored bar in Fig. 5 for $\mu = 1.5$, $v_0 = 0$: turquoise, and $\mu = 1.5$, $v_0 = 10$: pink). This structure is then assumed to be the best representation of the system for given parameters. If $p_s < 0.5$ we did not calculate the maximum (*e.g.* Fig. 5 for $\mu = 1.0$, $v_0 = 0$: all bars gray). Here, the system is predominantly in an unstructured state.

We then continued to calculate C_{max} while varying the self-propulsion speed v_0 and the magnetic strength μ and display C_{max} in a diagram of states (Fig. 6). The diagram of states shows that the structure depends on both the magnetic strength μ and the self-propulsion speed v_0 of the particles. For low magnetic strengths ($\mu \leq 1.0$) we observed no structure formation independent of the self-propulsion speed (as already shown in Fig. 3). For higher magnetic strengths, we observed chain and ring formation, depending on the self-propulsion speed. The results shown in Fig. 6 are qualitatively similar to bigger systems of dipolar active swimmers without confinement.[24] Importantly, by distinguishing the structured state more carefully (*i.e.* chains and rings) we can show that by changing the self-propulsion speed while keeping the magnetic strength constant one can influence the configuration of the dipolar swimmers. For example, the structure changes from a chain ($v_0 = 0$) to a ring ($v_0 = 5$) and back to a chain structure ($v_0 = 20$) while keeping the magnetic strength constant at $\mu = 1.5$.

One striking feature of the diagram of states is that there are two regions where chain structures are formed (for fixed μ these occur for small and large velocities, respectively). To study the
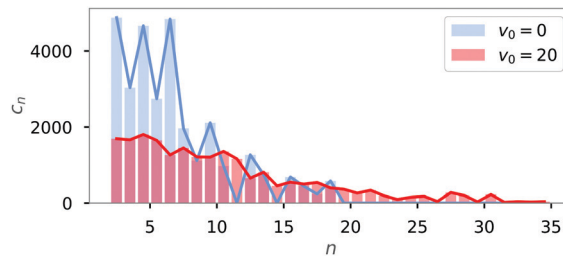
Fig. 7 Cluster-size distribution c_n of $N = 36$ particles in a quadratic box with $L = 50$ and $\alpha = 0$ for fixed magnetic strength $\mu = 1.5$ for passive ($v_0 = 0$) and active ($v_0 = 20$) particles. The case of passive particles is shown in blue and the one for active particles in red.

differences between these two scenarios for chains, *i.e.* between the passive ($v_0 = 0$) and the active ($v = 20$) chain configurations, we analyzed the cluster-size distribution c_n sorted by the cluster size n.

The distribution of cluster sizes is shown in Fig. 7 for fixed magnetic strength ($\mu = 1.5$). Passive particles (blue) tend to form many small clusters, while active particles (red) also form larger clusters of up to size $N = 36$.

3.3 Influence of wall geometry and its properties

In movies of the simulation, we noticed that the formation of rings is often initiated by collisions with walls. Therefore, we asked next how the formation of structures is affected by the walls of the system. We varied both the geometry and the type of interactions between the swimmer and the walls. Specifically, we considered that active particles tend to reorient at walls and added a wall torque, as previously introduced in eqn (3).

To analyze how the variation of the boundary conditions affects a single dipolar swimmer, we first simulated a single swimmer and analyzed the probability density. The results of ensemble and time averages over 243×10^6 snapshots are shown in Fig. 8 for squared and circular confinement and for three different torque parameters $\alpha = 0.0$; 0.4; 2.0.

We can identify two regions; a homogeneous probability density in the interior of the confinement ($r < R$), where the radial probability density is linear, and a second region directly at the side walls ($r = R$) or at the corners ($r = \sqrt{2}R$) of the confinement where the radial probability density drastically increases and shows peaks. With an additional wall induced torque ($\alpha \neq 0$), the relative probability density is increased in the interior with decreased peaks at the walls ($r = R$) or in the corners ($r = \sqrt{2}R$).

The relative probability density of one swimmer shows that active particles without a reorienting torque tend to get trapped at the boundaries, especially in the corners of a box. Introducing a wall torque results in a more homogeneous probability density, irrespective of the geometry. In the case of squared confinement, a high wall induced torque ($\alpha = 2$) prevents trapping in the corners. Trapping at the walls and in corners is reduced by the wall torque, as particles do not have to rely on thermal fluctuations for their reorientation.
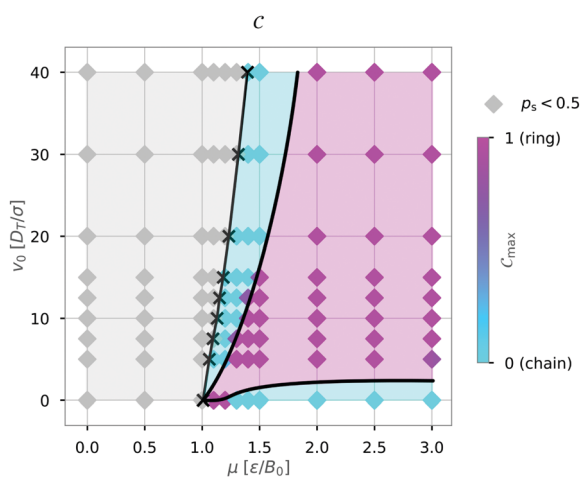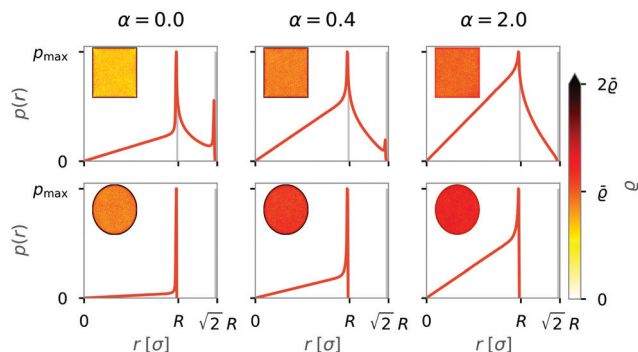

Fig. 6 Diagram of states for $N = 36$ particles in a quadratic box with $L = 50$ and $\alpha = 0$ according to the maximum of the order parameter C_{max}. Here, the magnetic strength μ and the self-propulsion speed v_0 are varied. The crosses indicate the critical magnetic moment μ^* for structure formation ($p_s = 0.5$) from Fig. 3. The colored areas and the lines were added as visual aids.

Fig. 8 Two-dimensional probability density (heat map in the inset) and radial probability density $p(r)$ for one swimmer in circular and squared confinement. The distributions were obtained from 243×10^6 snapshots of a single swimmer with speed $v_0 = 20$ (averaged over ensemble and time). The geometry (top row: squared, bottom row: circular) and the interactions with the walls were varied, using purely repelling walls ($\alpha = 0.0$) and walls with an additionally induced torque ($\alpha = 0.4$; 2.0). The side length of the box is $L = 50$. The radius of the circular confinement was chosen to match the area of the squared confinement. Volume that cannot be occupied by a swimmer is marked in gray. The color map is cut off at two times the average probability density $2\bar{\rho}$.

To test the hypothesis that ring formation is initiated by the walls of the confinement, we calculated the local order parameter $C_{\max}(r)$ for each position r on a 250 by 250 grid in the confinement over 10 realizations. The results for moderate swimming speed $v_0 = 15$ and magnetic strength $\mu = 2$ for different wall interactions and geometries are shown in Fig. 9. Rings (pink) form predominantly at the walls for the squared (top row) and the circular (bottom row) confinement, irrespective of the wall torque α. In the case of the squared confinement, ring formation also occurs in the corners of the confinement. These results illustrate that ring formation is predominantly caused by interactions with the walls of the confinement and that this mechanism is not strongly affected by the geometry or wall induced torques.
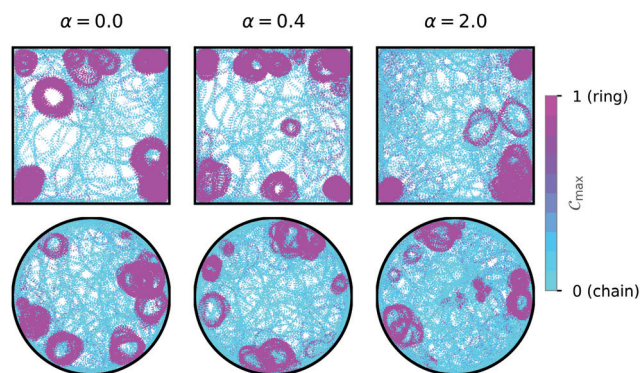

Fig. 9 Local order parameter $C_{\max}(r)$ for squared confinement (top row) and circular confinement (bottom row) with different induced wall torques $\alpha = 0.0$; 0.4; 2.0. The color bar represents the local order parameter. The local order parameter was calculated on a 250 by 250 grid for a self-propulsion speed $v_0 = 15$ and a magnetic strength $\mu = 2$ over 10 realizations. The side length of the box is $L = 50$ (circle $R = 50/\sqrt{\pi}$).

In addition, Fig. 9 suggest that rings are rather stationary, while chains remain motile. To analyze the dynamics of clusters systematically, we tracked the trajectories of individual clusters in chain ($C < 0.2$) or ring configuration ($C > 0.8$) and calculated the mean-squared displacement (MSD) of the center of geometry (cog) of these clusters. To extract the type of motion, we fitted the function $f(t) = 4D_{\text{cog}}t^{\nu}$ to these MSD curves,[55,56] using a least-squares method.[57] The MSD curves were obtained using a fast Fourier transform based implementation of a moving window algorithm.[58] To reduce the noise contributed by short-lived clusters on the MSD calculation, we analyzed configurations with a life time greater than $t_{\min} = 3.6$. Fig. 10 shows the fitted exponent ν and the prefactor D_{cog} against the order parameter C of the tracked clusters. For rings ($C > 0.8$), the exponent is mainly evenly distributed between 0.5 and 1.5, revealing that rings show diffusive behavior ($\nu = 1$) with some rings being sub- ($\nu < 1$) and superdiffusive ($\nu > 1$). For chains ($C < 0.2$) the exponent is distributed between 1 and 2 (while occurring more frequently at higher values of ν) which shows the superdiffusive behavior of chains. We note that truly ballistic motion ($\nu = 2$) is not reached. Since the exponent ν was determined over all available time scales, the typical diffusive behavior of active particles for short times contributes to reducing the measured exponents to $\nu < 2$. The low proportionality constant for rings proves together with the exponent ν that rings diffusive slowly or can be considered stationary ($D_{\text{cog}} \approx 0$) for the analyzed time scales. Chains on the other hand show superdiffusive motion where the factor D_{cog} increases with the self-propulsion velocity v_0, as expected.

Next, we ask the question how do these different wall geometries and wall properties affect structures globally? To answer that question we are again interested in the most representative structure formed by the dipolar swimmers. We therefore determined diagrams of states based on the maximum of the order parameter $C_{\max}$ while varying the boundary conditions. The results are shown in Fig. 11. The rows shows the dependence on the geometry (top row box, bottom row circle) and the columns the effect of the additional wall torque ($\alpha = 0.0$; 0.4; 2.0). The comparison between the diagrams of states shows that boundary conditions affect
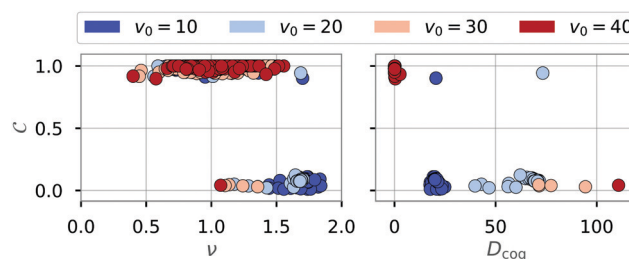

Fig. 10 Scatter plots of the exponent ν and the factor D_{cog} against the order parameter C obtained from mean-squared displacements of the center of geometry of clusters in either chain ($C < 0.2$) or ring ($C > 0.8$) configuration (we note that clusters with intermediate values of C were not included in this analysis). Data taken from 10 realizations of simulations for the parameters $v_0 = [10, 20, 30, 40]$ (blue to red), $\mu = [1.5, 2.0, 2.5, 3.0]$ for both circular and quadratic confinement with $L = 50$ and $\alpha = [0.0, 0.4, 2.0]$.
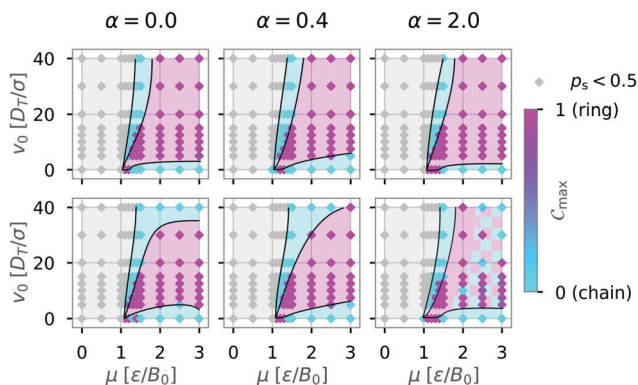
Fig. 11 Influence of the boundary conditions on the diagrams of states for $N = 36$ particles: The shape of the confinement (first row box $L = 50$, second row circle $R = 50/\sqrt{\pi}$) and the interactions with the walls (columns left to right: $\alpha = 0.0$; 0.4; 2.0) were varied and the diagram of states determined as in Fig. 6. The colored areas and the lines were added as visual aids. The hatched area indicates that no clear assignment to a dominant structure could be made for these parameters. Top left diagram shows same data as Fig. 6.

Fig. 12 Overview of the state weighted histograms of the order parameter C for circular confinement with $R = 50/\sqrt{\pi}$ and $\alpha = 2.0$ for $N = 36$ particles. The self-propulsion velocity v_0 and the magnetic strength μ are varied. The color bar indicates the dominant order parameter C_{max} corresponding to a chain (turquoise) or ring (pink) configuration. As in Fig. 5, if probability of structure formation $p_s < 0.5$ (inset) all bars remain gray. Data obtained from 10 independent simulations.

structure formation to some extent. Even though the mechanism of structure formation is not strongly affected by the geometry and wall induced torques, the relative frequency of chain and ring formation is affected.

Changing the geometry of the confinement while keeping the boundary conditions purely repulsive ($\alpha = 0.0$) seems to have the biggest impact on structure formation of dipolar swimmers. Here, we observe formation of chains (turquoise area) in the circular confinement for swimmers with high motility ($v_0 = 40$). The absence of corners in the circular environment removes the possibility for an already formed chain to get stuck in a corner and catch its own tail to form a ring. Hence, we observe fewer ring structures in a circular environment than in a squared one. Increasing the wall torque ($\alpha = 0.4$; 2.0) has no strong effect on structure formation in a squared confinement (top row). Yet, the diagram of states changes qualitatively with increasing wall torque for the case of the circular confinement (bottom row) where rings become more predominant with increasing wall torque. For large induced wall torques ($\alpha = 2.0$) a clear separation of ring and chain states can no longer be made in the case of circular confinement (hatched area).

To gain more information about this hatched area, we took a closer look at the histograms of the order parameter for a circular confinement with a wall torque parameter $\alpha = 2.0$ (see Fig. 12). Here, we observed maxima of chain configurations with $C_{max} \neq 0$ as well as bimodal distributions with two peaks for chain and ring configurations of approximately the same height ($v_0 = 20$, $\mu = 2.5$). These observations can explain the heterogeneity of the order parameter in the hatched area.

3.4 Influence of density

In this section we discuss how density affects cluster formation. We modulated the density by increasing the particle number, as well as by reducing the size of the simulation box. So far all
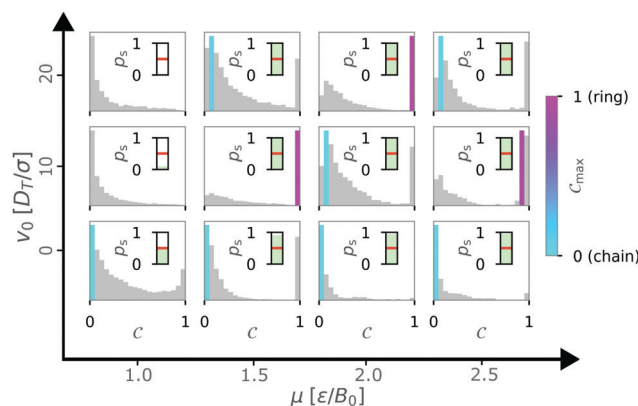
the simulations were done for $N = 36$ particles. Now, we ask how increasing the density by increasing the particle number affects structure formation. To answer this question, we increased the particle number to $N = 81$ particles with a box size of $L = 50$ ($\Phi = 0.03$) for different geometries and wall interactions. For a systematic analysis, we repeated the calculation of the order parameter C and determined diagrams of states (see Fig. 13) as before.

We noticed that the diagram of states are similar to the simulations with $N = 36$ particles (see Fig. 11). Specifically, the transition from no structure (gray) to any structure (turquoise and pink) is approximately the same. However, there are differences in the regions with structures. We no longer see a clear chain regime for the passive case ($v_0 = 0$), instead the C_{max} values indicate more heterogeneous structures. Inspection of the histograms of the order parameter C (Fig. 14) shows that for higher particle number the histograms are multi-modal and
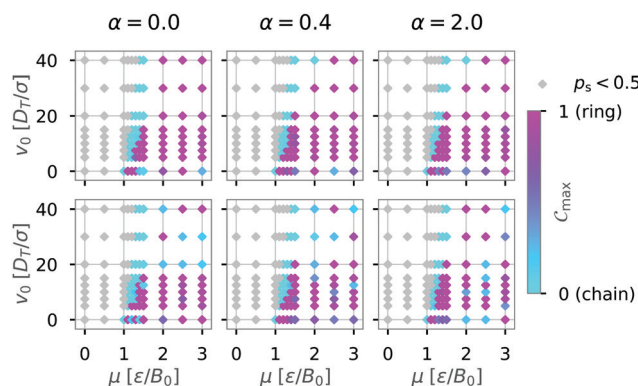

Fig. 13 Diagram of states according to the order parameter C_{max} for $N = 81$ particles and different boundary conditions (top row: box confinement $L = 50$), bottom row: circular confinement $R = 50/\sqrt{\pi}$, columns: different values of wall torque parameter α. The color bar represents the order parameter.
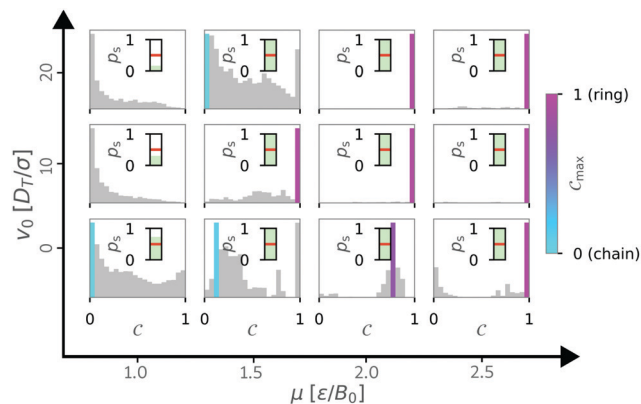
Fig. 14 State weighted histograms of the order parameter C for $N = 81$ particles in squared confinement with $L = 50$ and $\alpha = 0$ for varying self-propulsion velocity v_0 and the magnetic strength μ. The color bar represents the dominant order parameter C_{max}, corresponding to a chain (turquoise) or ring (pink) configuration. As in Fig. 5, if $p_s < 0.5$ (inset) all bars remain gray.

that maxima can occur at intermediate values of C (*cf.* $\mu = 2.0$ and $v_0 = 0$). These observations suggest that also intermediate structures like bend chains or almost closed rings can be present.

However, we noticed that next to the previously seen chain and ring structures more complex structures, such as branches or loops within a ring can emerge in simulations with $N = 81$ particles. Selected examples for these complex structures are shown in Fig. 15. Such structures are also known from systems of passive particles[28] and indeed they appear to be more frequent for values of $v_0 = 0$, as indicated by the higher occurrence of intermediate values of C in the histograms (see Fig. 14). However, some of these complex structures cannot be properly characterized by our order parameter C, since the head–tail distance is no longer well defined, and other ways of characterizing them have to be developed.

In addition, we modulated the density by reducing the box size of the squared confinement with $N = 36$ particles and

Fig. 15 A selection of complex structures that were observed in systems with $N = 81$ particles (with different self-propulsion velocities and magnetic strengths). The direction of the magnetic moment is indicated by a black arrow. Branches, chains with loops and rings with multiple loops or multiple rings in one structure are shown.
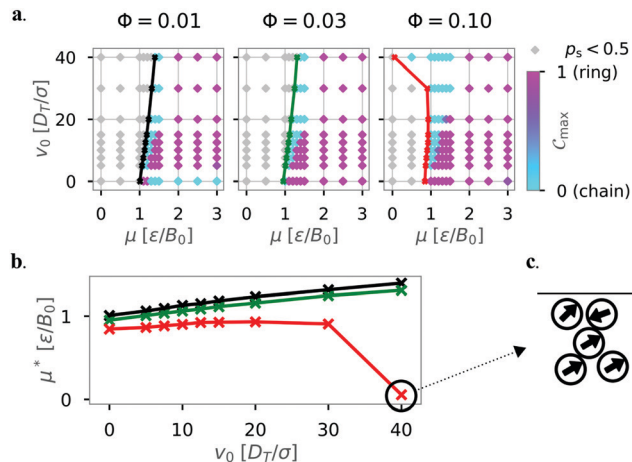

Fig. 16 (a) Diagram of states according to the order parameter C_{max} for $N = 36$ particles in squared confinement with $\alpha = 0$ for different densities Φ by reducing the box size L. The colored line shows the critical magnetic strength in the diagram of states. The color bar represents the order parameter. Data taken over 10 independent simulations. Top left diagram shows same data as Fig. 6. (b) Critical magnetic strength μ^* against the self-propulsion velocity v_0. The colors indicate the different densities $\Phi = 0.01$ ($L = 50$, black), $\Phi = 0.03$ ($L = 33.3$, green), and $\Phi = 0.10$ ($L = 16.8$, red). (c) Extract from a snapshot showing a disordered cluster formed in the top right corner of the squared confinement for the parameters $\mu = 0$, $v_0 = 40$.

purely repelling walls ($\alpha = 0$) to $L = 33.3$ ($\Phi = 0.03$, matching the density of the system with $N = 81$, $L = 50$) and $L = 16.8$ ($\Phi = 0.1$) respectively. Fig. 16 shows how the diagram of states (a) and the critical magnetic strength μ^* for structure formation (b) are affected by the reduced box size. In smaller systems (with increasing density) ring structures become dominant for passive particles ($v_0 = 0$). This result is very similar, but not exactly the same as for the system with $N = 81$ particles and matching density (see Fig. 13 top left, where differences between the two realizations of the same density are seen for small v_0). Furthermore, chain structures become dominant for high motilities for $\mu < 1.0$ in the case of $\Phi = 0.10$. This finding is in agreement with the recent results of Liao *et al.*, who showed that the probability of chain formation is increased because of smaller mean separation between the particles for higher densities.[24] This explanation is confirmed by the observed shift of the critical magnetic strength with increasing density (Fig. 16b).

A striking deviation from this linear behavior is seen for high motility in the smallest system ($L = 16.8$, $\Phi = 0.10$, red line) where structures are formed without magnetic interactions ($\mu^* \approx 0$). This deviation occurs when the persistence length of the swimmers is much greater than the dimensions of the confining walls $v_0/D_R \gg L$. Here, the formed clusters are qualitatively different from the previously observed chains and rings (see Fig. 16c). These particles form rather disordered, finite-sized clusters at the walls of the squared confinement ($\alpha = 0$). The clusters are similar to clusters observed for active systems that display motility-induced phase separation (MIPS).[59,60] In our system, the presence of boundaries seems to take the role of high density clusters during MIPS. We note

that the system densities presented in this study are well below the critical density where MIPS is expected.[61] It was shown recently that MIPS is repressed by strong dipolar interactions between particles for larger systems with higher densities.[24]

4 Conclusions

In this study, we used Brownian dynamics simulations to address self-assembly of dipolar active particles in small systems under confinement. We mainly observed chain and ring formation and investigated how self-assembly depends on self-propulsion speed v_0 and magnetic strength μ of the particles. In the following, we will summarize our three main results.

First, we calculated the probability of the swimmers to self-assemble into structures, also known as the degree of polymerization, while varying those two parameters. We showed that a critical magnetic strength μ^* can be defined. This critical magnetic strength increases linearly with the self-propulsion velocity. This finding suggests that, at least to some extent, the activity of the particles might be treated as an effective temperature in further studies.

Second, we then defined an order parameter that is able to distinguish between chain and ring configurations and showed in a diagram of states what configurations are most likely to occur depending on v_0 and μ. Generally, the configurations depend on motility and magnetic strength, which is in qualitative agreement with studies of bigger systems.[24] In addition, we showed that ring configurations dominate the diagram of states for the analyzed parameters. An analysis of the dynamics of the clusters in chain and ring configuration revealed that chains are motile structures with superdiffusive behavior while rings remain stationary with mainly (sub-)diffusive behavior and a very small diffusion coefficient. When analyzing systems with $N = 81$ particles, we observed more complex structures like branches or loops within a ring; different order parameters will be needed to characterize these structures properly. Since the considered systems are quite small, we saw that increasing the density by increasing the particle number or by reducing the size of the confinement do not result in exactly the same diagrams of states.

Third, we studied the effect of geometry and wall properties on the structures. We introduced a circular geometry and a reorienting torque at the walls. By calculating a local order parameter, we showed that ring configurations dominantly occur at walls, independent of the geometry or the properties of the wall. This finding suggests that already assembled chains collide with the walls which then causes ring formation. Comparing the diagrams of states, we see that the structure is indeed affected by both the geometry of confinement and the wall torque, but the effect of the geometry is dominant. Chain configurations seem to be preferred for high motility in circular confinement.

Taken together our results show that dipolar interactions of active particles such as in magnetic active particles can lead to a rich variety of structures that self-organize. Interactions with confining walls have an important influence on these structures. Thus an understanding of the interactions in any specific system of active particles is required for understanding and predicting structure formation in that system.

Conflicts of interest

There are no conflicts to declare.

Acknowledgements

References

1 P. Romanczuk, M. Bär, W. Ebeling, B. Lindner and L. Schimansky-Geier, *Eur. Phys. J.: Spec. Top.*, 2012, **202**, 1–162.

2 T. Vicsek and A. Zafeiris, *Phys. Rep.*, 2012, **517**, 71–140.

3 C. Bechinger, R. Di Leonardo, H. Löwen, C. Reichhardt, G. Volpe and G. Volpe, *Rev. Mod. Phys.*, 2016, **88**, 45006.

4 J. Elgeti, R. G. Winkler and G. Gompper, *Rep. Prog. Phys.*, 2015, **78**, 56601.

5 K. E. Peyer, L. Zhang and B. J. Nelson, *Nanoscale*, 2013, **5**, 1259–1272.

6 K. Bente, A. Codutti, F. Bachmann and D. Faivre, *Small*, 2018, **14**, 1704374.

7 D. A. Bazylinski and R. B. Frankel, *Nat. Rev. Microbiol.*, 2004, **2**, 217–230.

8 D. Faivre and D. Schüler, *Chem. Rev.*, 2008, **108**, 4875–4898.

9 R. B. Frankel and D. A. Bazylinski, in *Contributions to Microbiology*, ed. M. Collin and R. Schuch, Karger, New York, Basel, 2009, vol. 16, pp. 182–193.

10 S. Klumpp and D. Faivre, *Eur. Phys. J.: Spec. Top.*, 2016, **225**, 2173–2188.

11 S. Klumpp, C. T. Lefèvre, M. Bennet and D. Faivre, *Phys. Rep.*, 2019, **789**, 1–54.

12 A. Codutti, K. Bente, D. Faivre and S. Klumpp, *PLoS Comput. Biol.*, 2019, **15**, e1007548.

13 R. B. Frankel, R. P. Blakemore and R. S. Wolfe, *Science*, 1979, **203**, 1355–1356.

14 S. K. Alsaiari, A. H. Ezzedine, A. M. Abdallah, R. Sougrat and N. M. Khashab, *OpenNano*, 2016, **1**, 36–45.

15 M. M. Stanton, B.-W. Park, D. Vilela, K. Bente, D. Faivre, M. Sitti and S. Sánchez, *ACS Nano*, 2017, **11**, 9968–9978.

16 O. Felfoul, M. Mohammadi, S. Taherkhani, D. De Lanauze, Y. Zhong Xu, D. Loghin, S. Essa, S. Jancik, D. Houle, M. Lafleur, L. Gaboury, M. Tabrizian, N. Kaou, M. Atkin, T. Vuong, G. Batist, N. Beauchemin, D. Radzioch and S. Martel, *Nat. Nanotechnol.*, 2016, **11**, 941–947.

17 J. Yan, S. C. Bae and S. Granick, *Adv. Mater.*, 2015, **27**, 874–879.

18 G. Steinbach, M. Schreiber, D. Nissen, M. Albrecht, E. Novak, P. A. Sánchez, S. S. Kantorovich, S. Gemming and A. Erbe, *Phys. Rev. E: Stat., Nonlinear, Soft Matter Phys.*, 2019, **100**, 012608.

19 R. Dreyfus, J. Baudry, M. L. Roper, M. Fermigier, H. A. Stone and J. Bibette, *Nature*, 2005, **437**, 862–865.

20 L. Zhang, J. J. Abbott, L. Dong, B. E. Kratochvil, D. Bell and B. J. Nelson, *Appl. Phys. Lett.*, 2009, **94**, 64107.

21 J. Hernández-Rojas, D. Chakrabarti and D. J. Wales, *Phys. Chem. Chem. Phys.*, 2016, **18**, 26579–26585.

22 A. Kaiser, K. Popowa and H. Löwen, *Phys. Rev. E: Stat., Nonlinear, Soft Matter Phys.*, 2015, **92**, 012301.

23 S. H. L. Klapp, *Curr. Opin. Colloid Interface Sci.*, 2016, **21**, 76–85.

24 G.-J. Liao, C. K. Hall and S. H. L. Klapp, *Soft Matter*, 2020, **16**, 2208–2223.

25 D. Levesque and J. J. Ewis, *Mol. Phys.*, 1982, **45**, 733–746.

26 S. H. L. Klapp, *J. Phys.: Condens. Matter*, 2005, **17**, R525–R550.

27 J. J. Weis and D. Levesque, *Adv. Polym. Sci.*, 2005, **185**, 163–225.

28 P. G. de Gennes and P. A. Pincus, *Phys. Kondens. Mater.*, 1970, **11**, 189–198.

29 I. S. Jacobs and C. P. Bean, *Phys. Rev.*, 1955, **100**, 1060–1067.

30 R. Messina, L. A. Khalil and I. Stanković, *Phys. Rev. E: Stat., Nonlinear, Soft Matter Phys.*, 2014, **89**, 011202.

31 R. Messina and I. Stanković, *Europhys. Lett.*, 2015, **110**, 46003.

32 B. Kiani, D. Faivre and S. Klumpp, *New J. Phys.*, 2015, **17**, 43007.

33 F. Guzmán-Lastra, A. Kaiser and H. Löwen, *Nat. Commun.*, 2016, **7**, 13519.

34 J. Toner, Y. Tu and S. Ramaswamy, *Ann. Phys.*, 2005, **318**, 170–244.

35 A. P. Berke, L. Turner, H. C. Berg and E. Lauga, *Phys. Rev. Lett.*, 2008, **101**, 038102.

36 M. B. Wan, C. J. Olson Reichhardt, Z. Nussinov and C. Reichhardt, *Phys. Rev. Lett.*, 2008, **101**, 18102.

37 G. Li and J. X. Tang, *Phys. Rev. Lett.*, 2009, **103**, 078101.

38 M. C. Marchetti, J. F. Joanny, S. Ramaswamy, T. B. Liverpool, J. Prost, M. Rao and R. A. Simha, *Rev. Mod. Phys.*, 2013, **85**, 1143–1189.

39 K. Drescher, *Biological Microswimmers, in Microswimmers – From Single Particle Motion to Collective Behaviour*, ed. G. Gompper, C. Bechinger, S. Herminghaus, R. Isele-Holder, U. B. Kaupp, H. Löwen, H. Stark and R. G. Winkler, Forschungszentrum Jülich GmbH Zentralbibliothek, Jülich, 2015, pp. B2.5–B2.6.

40 J. P. Hernandez-Ortiz, P. T. Underhill and M. D. Graham, *J. Phys.: Condens. Matter*, 2009, **21**, 204107.

41 T. Ostapenko, F. J. Schwarzendahl, T. J. Böddeker, C. T. Kreis, J. Cammann, M. G. Mazza and O. Bäumchen, *Phys. Rev. Lett.*, 2018, **120**, 68002.

42 P. Sartori, E. Chiarello, G. Jayaswal, M. Pierno, G. Mistura, P. Brun, A. Tiribocchi and E. Orlandini, *Phys. Rev. E: Stat., Nonlinear, Soft Matter Phys.*, 2018, **97**, 022610.

43 K. W. Yung, P. B. Landecker and D. D. Villani, *Magn. Electr. Sep.*, 1998, **9**, 39–52.

44 D. Chandler, J. D. Weeks and H. C. Andersen, *Science*, 1983, **220**, 787–794.

45 K. W. Yung, P. B. Landecker and D. D. Villani, *Magn. Electr. Sep.*, 1999, **10**, 29–33.

46 G. Volpe, I. Buttinoni, D. Vogt, H. J. Kümmerer and C. Bechinger, *Soft Matter*, 2011, **7**, 8810–8815.

47 V. Kantsler, J. Dunkel, M. Polin and R. E. Goldstein, *Proc. Natl. Acad. Sci. U. S. A.*, 2013, **110**, 1187–1192.

48 R. L. Honeycutt, *Phys. Rev. A: At., Mol., Opt. Phys.*, 1992, **45**, 600–603.

49 P. E. Kloeden and E. Platen, *J. Stat. Phys.*, 1992, **66**, 283–314.

50 F. Pedregosa, G. Varoquaux, A. Gramfort, V. Michel, B. Thirion, O. Grisel, M. Blondel, P. Prettenhofer, R. Weiss, V. Dubourg, J. Vanderplas, A. Passos, D. Cournapeau, M. Brucher, M. Perrot and É. Duchesnay, *J. Mach. Learn. Res.*, 2011, **12**, 2825–2830.

51 H. Schmidle, C. K. Hall, O. D. Velev and S. H. Klapp, *Soft Matter*, 2012, **8**, 1521–1531.

52 S. Sarkar Das, A. Ploplis Andrews and S. C. Greer, *J. Chem. Phys.*, 1995, **102**, 2951–2959.

53 J. Stambaugh, K. Van Workum, J. F. Douglas and W. Losert, *Phys. Rev. E: Stat., Nonlinear, Soft Matter Phys.*, 2005, **72**, 031301.

54 L. L. C. Gurobi Optimization, *Gurobi Optimizer Reference Manual*, 2020, http://www.gurobi.com.

55 J. P. Bouchaud and A. Georges, *Phys. Rep.*, 1990, **195**, 127–293.

56 R. Metzler and J. Klafter, *Phys. Rep.*, 2000, **339**, 1–77.

57 P. Virtanen, R. Gommers, T. E. Oliphant, M. Haberland, T. Reddy, D. Cournapeau, E. Burovski, P. Peterson, W. Weckesser, J. Bright, S. J. van der Walt, M. Brett, J. Wilson, K. J. Millman, N. Mayorov, A. R. Nelson, E. Jones, R. Kern, E. Larson, C. J. Carey, L. Polat, Y. Feng, E. W. Moore, J. VanderPlas, D. Laxalde, J. Perktold, R. Cimrman, I. Henriksen, E. A. Quintero, C. R. Harris, A. M. Archibald, A. H. Ribeiro, F. Pedregosa, P. van Mulbregt, A. Vijaykumar, A. P. Bardelli, A. Rothberg, A. Hilboll, A. Kloeckner, A. Scopatz, A. Lee, A. Rokem, C. N. Woods, C. Fulton, C. Masson, C. Häggström, C. Fitzgerald, D. A. Nicholson, D. R. Hagen, D. V. Pasechnik, E. Olivetti, E. Martin, E. Wieser, F. Silva, F. Lenders, F. Wilhelm, G. Young, G. A. Price, G. L. Ingold, G. E. Allen, G. R. Lee, H. Audren, I. Probst, J. P. Dietrich, J. Silterra, J. T. Webber, J. Slavič, J. Nothman, J. Buchner, J. Kulick, J. L. Schönberger, J. V. de Miranda Cardoso, J. Reimer, J. Harrington, J. L. C. Rodríguez, J. Nunez-Iglesias, J. Kuczynski, K. Tritz, M. Thoma, M. Newville, M. Kümmerer, M. Bolingbroke, M. Tartre, M. Pak, N. J. Smith, N. Nowaczyk, N. Shebanov, O. Pavlyk, P. A. Brodtkorb, P. Lee, R. T. McGibbon, R. Feldbauer, S. Lewis, S. Tygier, S. Sievert, S. Vigna, S. Peterson, S. More, T. Pudlik, T. Oshima, T. J. Pingel, T. P. Robitaille, T. Spura, T. R. Jones, T. Cera, T. Leslie, T. Zito, T. Krauss, U. Upadhyay, Y. O. Halchenko and Y. Vázquez-Baeza, *Nat. Methods*, 2020, **17**, 261–272.

58 V. Calandrini, E. Pellegrini, P. Calligari, K. Hinsen and G. Kneller, *École thématique de la Société Française de la Neutronique*, 2011, **12**, 201–232.

59 I. Buttinoni, J. Bialké, F. Kümmel, H. Löwen, C. Bechinger and T. Speck, *Phys. Rev. Lett.*, 2013, **110**, 238301.

60 M. E. Cates and J. Tailleur, *Annu. Rev. Condens. Matter Phys.*, 2015, **6**, 219–244.

61 P. Digregorio, D. Levis, A. Suma, L. F. Cugliandolo, G. Gonnella and I. Pagonabarraga, *Phys. Rev. Lett.*, 2018, **121**, 98003.